NEXRES 2 (2025) 100983

Contents lists available at ScienceDirect

Next Research

journal homepage: www.elsevier.com/locate/nexres

Colorimetric detection and removal of copper(II) ions from wastewater using a Griess reagent and cellulose nanofibers supported with mesoporous silica nanoparticles: An ImageJ and CIELAB colour space-based analytical approach

Aneswa M. Ninela [a], Sindisiwe F. Shange [a], Asanda Mtibe [b], Jerome E. Andrew [c], Thabang H. Mokhothu [a,d,*]

[a] Department of Chemistry, Durban University of Technology, Durban, South Africa
[b] Centre for Nanostructures and Advanced Materials, Chemicals Cluster, CSIR, Pretoria, South Africa
[c] Biorefinery Industry Development Facility (BIDF), CSIR, Durban, South Africa
[d] Faculty of Agricultural and Natural Sciences, University of Mpumalanga, Mbombela, South Africa

ARTICLE INFO

Keywords:
Adsorption
Cellulose nanofibers
CIELAB
Cu(ii)
ImageJ
Mesoporous silica nanoparticles
Wastewater

ABSTRACT

This study presents a green, cost-effective, and dual-function approach for the colorimetric detection and removal of copper ions (Cu(II)) in wastewater, utilizing a cellulose nanofiber–mesoporous silica nanoparticle (CNF-MSN) composite in conjunction with the Griess reagent. The CNF-MSN composite was synthesized via a sol–gel process using cellulose nanofibers derived from natural biomass. Comprehensive characterization using FTIR, SEM, XRD, BET, TEM, and TGA confirmed the successful integration of CNF and MSN, with TEM revealing a web-like nanofiber structure (~33 nm) and SEM showing mesoporous silica nanoparticles (2–50 nm). Hydrogen bonding between CNF hydroxyl groups and MSN silanol groups was indicated by O–H stretching shifts. For Cu(II) detection, the CNF-MSN composite produced a visible purple color change upon reaction with the Griess reagent across 1–5 mg/L Cu(II) standards. Color intensity and RGB values were quantified using ImageJ, converted to CIEXYZ and CIELAB (Lab) values, resulting in a linear response ($R^2 = 0.9956$) over the range of 0.01–5 mg/L, with a detection limit of 0.001521 mg/L. The UV–Vis spectrophotometric method validated the ImageJ approach, yielding an R^2 value of 0.9993 and a detection limit of 0.006253 mg/L. For Cu(II) adsorption, CNF-MSN removed nearly 100 % of Cu(II) within 45 min at pH 4–6, outperforming individual CNF and MSN with an adsorption capacity of 0.0978 mg/g and 97.85 % removal efficiency. In real samples, removal efficiencies ranged from 94.1 % to 99.1 %, with a maximum adsorption capacity of 38.9 mg/g. The adsorption data fit the Dubinin–Radushkevich isotherm ($R^2 = 0.980$) and the pseudo-second-order kinetics ($R^2 = 0.999$). Overall, the CNF-MSN composite offers a sustainable and efficient material for detecting and remediating Cu(II) in water systems.

1. Introduction

Cellulose nanofibers (CNF) have a variety of potential applications, including biomedical and pharmaceutical uses (such as tissue engineering), packaging, and the paper and film industries [1]. In environmental management, the focus has shifted towards polymer science-derived polymeric materials, such as cellulose, to solve environmental problems, i.e., cleaning wastewater. Cellulose-based materials garner significant interest for their applications in environmental remediation, particularly in water purification. However, these materials demonstrated drawbacks, including the partial removal of contaminants from wastewater. To mitigate this problem, developing an eco-friendly composite adsorbent through an environmentally friendly process for detecting and removing metal ions from wastewater is urgently necessary, as metal ions pose critical hazards to public health and environmental safety [2,3]. This approach includes fabricating organic-inorganic nanohybrids by coupling cellulosic material with metal oxide, such as copper oxide (CuO), and silica oxide (SiO_2)

* Corresponding author.
E-mail address: thabang.mokhothu@ump.ac.za (T.H. Mokhothu).

https://doi.org/10.1016/j.nexres.2025.100983
Received 13 August 2025; Received in revised form 20 October 2025; Accepted 27 October 2025
Available online 28 October 2025

nanoparticles (NPs) [4]. This has demonstrated growth in the field of biomedical materials [5,6], food packaging [7], textiles [8], and water purification [9]. The unique properties of CNF, including a high aspect ratio, lower density, and biocompatibility, have enabled them to excel and have generated significant interest in various fields [1]. The presence of the OH-functional group in the CNF structure enables the introduction of cationic groups, thereby enhancing their adsorption capability as adsorbents. Cellulosic materials, and their derivatives, coupled with inorganic nanoparticles, have shown promising results [10].

The growing concern for sustainability and environmental preservation has increased the demand for low-cost, fast-response, and reliable devices to monitor the presence of heavy metals and toxins in water bodies before they are removed [11–13]. Among various methods studied for removing and monitoring heavy metals from water, adsorption has been considered a suitable method. This is due to high efficiency [14], simplicity, and low cost [15]. Numerous researchers have investigated the use of eco-friendly adsorbents as alternatives to traditional adsorbents [15–18]. Cellulose has recently gained considerable attention due to its eco-friendliness, cost-effectiveness, non-toxicity, selectivity, and high efficiency [19]. However, cellulose exhibits strong hydrogen bonding between hydroxyl groups, which increases its crystallinity and thereby limits the adsorption capacity of heavy metals in water [16]. To address these drawbacks, cellulose can be modified to enhance the adsorption performance. Although the modification of cellulose for heavy metals adsorption has been extensively studied, to the best of our knowledge, there is little information in the literature on the modification of cellulose nanofibers with mesoporous silica nanoparticles for water purification. At the same time, isotherms and isotherm models have not been thoroughly explored. This study aims to synthesize cellulose nanofibers supported by mesoporous silica nanoparticles as a promising detector and adsorbent of heavy metals in wastewater. Furthermore, a novel detection method using colour-space models will be explored.

Various detection methods have been formulated for quantifying colour and expressing colour numerically [2,20]. A colour space defined by the International Commission on Illumination (CIE) represents colour using three values: L* (lightness), a* (red-green), and b* (yellow-blue) (CIE L*a*b*). This colour space has also emerged for quantifying effluent colours in wastewater [21]. Most instruments used for determining heavy metals are spectroscopic instruments, such as atomic absorption spectrometry, X-ray fluorescence, plasma emission spectroscopy, dispersive liquid–liquid microextraction, UV–visible spectrophotometry, solid-phase extraction, and Inductively Coupled Plasma Optical Emission Spectroscopy (ICP-OES) [20,22,23]. The application of CIE L*a*b*/Yxy colour space based on the combination of TRPIDA_CH_3-AuNPs to quantify Cr(VI) in wastewater effluent was investigated by Muthwa et al. 2020. The synthesised colorimetric sensor exhibited high sensitivity to Cr(VI) in aqueous solutions and demonstrated pleasing selectivity over the investigated metal ions [24]. This colour space enabled the detection of subtle colour changes that were not visible to the naked eye [25]. The sensing approach has also been employed in the detection of Cu(II), Ni(II), Zn(II), Cd(II), and Pb(II) ions in natural water using PVC membranes, and in potable water through nanocomposites incorporating multi-walled carbon nanotubes (MWCNTs) and polylactic acid (PLA) nanofibers [26,27]. In another study, the colorimetric method was further optimised for detecting gold nanoparticles in water using polyDADMAC, with colour analysis performed through the CIE Lab*/Yxy colour space system [28]. Sadollahkhani et al. conducted a study on the detection of copper using a fabricated ZnO@ZnS core–shell nanoparticle-based paper sensor [29,30]. The paper sensor was tested on real river water with turbulent flow and showed a maximum relative error of 5 % in determining the concentration of Cu(II) ions. This confirmed that the paper sensor can efficiently detect complex solutions with high selectivity. Additionally, colour-space models can quantify colours in various ways, including CIELAB, CMYK, RGB, HSL, and XYZ [31,32].

ImageJ has emerged as a critical tool in the analysis of heavy metal contamination, particularly in environmental studies, and its application in detecting and quantifying Cr(VI), Mn(II), and Co(II) [28]. Kubheka et al. (2025) employed ImageJ software to quantify lead ion (Pb (II)) concentrations in environmental water using gold nanoparticles (AuNPs) as a colorimetric probe [33]. Similarly, Kant et al. highlighted advances in developing portable chemical sensing devices for detecting heavy metals, anions, and biomolecules. Therefore, this study focused on environmental concerns by creating a colorimetric sensor and an adsorbent composite from cellulose derived from agricultural by-products, wood pulp, coupled with mesoporous silica nanoparticles, to address the pollution of Cu(II) metal ions in municipal wastewater. In this study, cellulose nanofibers were extracted mechanically, and mesoporous silica nanoparticles (MSNs) and MSN—CNFs were synthesized using an in-situ sol-gel technique. Fourier transform infrared spectroscopy (FTIR), scanning electron microscopy (SEM), X-ray diffraction (XRD), Brunauer–Emmett–Teller surface area analysis (BET), transmission electron microscopy (TEM), and thermogravimetric analysis (TGA) were then used to analyse the samples.

2. Materials and methods

CNF derived from wood pulp was supplied by the Council for Scientific and Industrial Research (CSIR), South Africa. Sodium hydroxide (NaOH) pellets (99.9 %), potassium hydroxide (KOH) pellets (98 %), and sodium chlorite ($NaClO_2$, 99.9 %) were obtained from Minema and used without further purification. Cetyltrimethylammonium bromide (CTAB) and tetraethyl orthosilicate (TEOS) were purchased from Sigma-Aldrich. Ethanol, methanol, and nitric acid (HNO_3) were also used as received from Minema. Copper nitrate [$Cu(NO_3)_2{\cdot}3H_2O$] was obtained from Sigma-Aldrich. All materials were of high purity and were used as received without further purification.

2.1. Preparation of CNF from wood pulp supplied by CSIR

A suspension of 1 wt.% pulp was made by first dispersing the pulp fibres in water using a mechanical stirrer (Lorentzen & Wettre Pulp Disintegrator, Sweden) set at 2000 rpm for 30 min. The pulp suspension was passed through a super-mass colloider (Masuko Sangyo Co., Ltd, Japan) set at 2507 rpm for 200 passes in the contact mode to obtain the nanofibers.

2.2. Synthesis of mesoporous silica nanoparticles

The *in situ* sol-gel method described by [34] was modified to synthesise MSNs. Tetraethyl orthosilicate (TEOS) was used as a silica precursor, and cetyltrimethylammonium bromide (CTAB) as a surfactant. Mesoporous silica nanoparticles were synthesized from the addition of ethanol (EtOH), water (H_2O), and catalyst 2 M NaOH (1:4:4:3.5 mol ratio), respectively, followed by the addition of CTAB (1 g), and the reaction was maintained under vigorous stirring for 30 min at 60 °C (Fig. 1). The removal of the surfactant was achieved by stirring a 1:1 ratio of water and methanol overnight.

2.3. Synthesis of CNF-MSN composite

The CNF-MSN composite was synthesised using an in-situ sol-gel approach. CNFs (1 wt.%) were dispersed in deionised water using ultrasonication for 30 min. The MSN precursor solution, prepared as described in Section 2.1, was added dropwise to the CNF dispersion under constant stirring at 80 °C for 3 h (Fig. 2). The hybrid CNF-MSN material was then centrifuged, washed with ethanol, and dried at 60 °C for 12 h. The surfactant was removed by stirring a 1:1 ratio of water and methanol overnight.

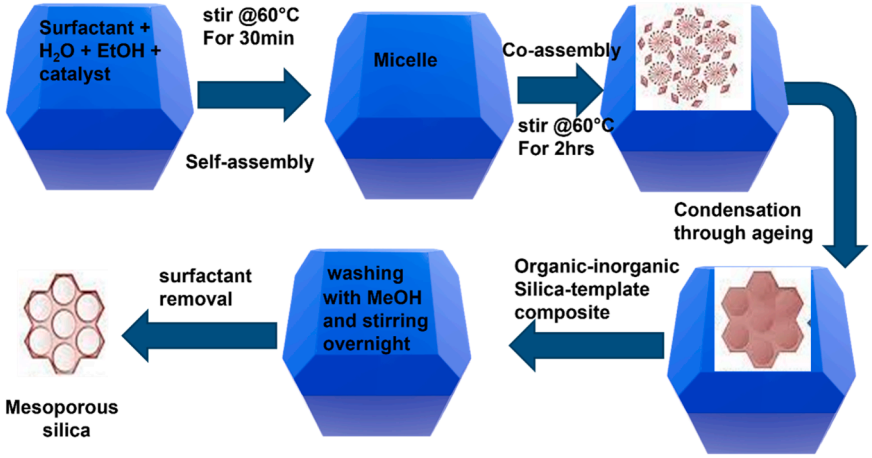

Fig. 1. Schematic diagram for the synthesis of MSN by the sol-gel method.

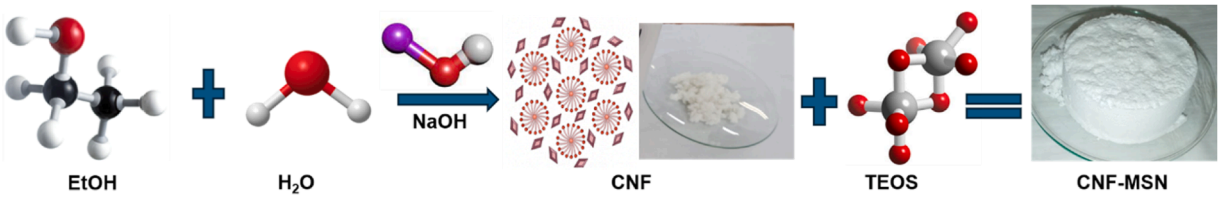

Fig. 2. Preparation process of CNF-MSN composite.

2.4. Characterization of CNF, MSN, and CNF-MSN

2.4.1. Transmission electron microscope (TEM)

The dimensions of CNF were measured using a JEOL JEM 2100 HRTEM (JEOL, Tokyo, Japan). CNF were imaged at a voltage of 200 kV, and the images were captured using a Gatan Ultra scan camera and Digital Micrograph software (Gatan, Pleasanton, CA, USA).

2.4.2. Scanning electron microscope (SEM)

The surface morphology of MSN was investigated using a scanning electron microscope (SEM; JEOL JSM 7500F, Tokyo, Japan). The MSN was imaged at an accelerating voltage of 3 kV, and the images were captured using image analysis software (ImageJ, National Institute of Health, Bethesda, MD, USA).

2.4.3. Attenuated total reflection Fourier transform infrared (ATR-FTIR)

The ATR-FTIR spectra of the CNF, MSN, and CNF-MSN were determined by an ATR-FTIR 4000 spectrophotometer (PerkinElmer, Waltham, Massachusetts, United States of America). All materials were analysed over a range of 4000–500 cm^{-1} with an average of 32 scans and a resolution of 4 cm^{-1}.

2.4.4. X-ray diffraction (XRD)

The XRD profiles of CNF, MSN, and CNF-MSN were obtained using an Anton Paar SAXSess (Anton Paar, Graz, Austria) operating at 40 kV and 50 mA in line collimation. The XRD radiation was Cu Kα radiation of wavelength 0.154 nm, and the exposure time of each material was 10 min. The scattering radiation was detected at a 2θ range of 5–80° at a rate of 1 s per step.

2.4.5. Thermogravimetric analysis (TGA)

TGA analysis of CNF, MSN, and CNF-MSN was performed on a thermogravimetric analyzer (PerkinElmer, Buckinghamshire, UK) at a heating rate of 10 °C/min using nitrogen as the purge gas. The TGA temperatures increased linearly from room temperature to 900 °C under nitrogen flow. The temperature of the sample was monitored, and the sample's weight loss was presented as a percentage weight loss.

2.4.6. Brunauer-Emmett-Teller (BET) analysis

The surface area, average pore size, and pore volume of CNF, MSN, and CNF-MSN were measured by Brunauer-Emmett-Teller (BET, Micromeritics TriStar II, Germany) analyzer.

2.5. Preparation of colorimetric sensor (Griess reagent)

A method previously employed for fabricating a nitrite sensor based on the adsorption of the Griess reagent onto MSN [35] was adopted in this study to prepare a Griess reagent composite using CNF-MSN (Fig. 3). The original procedure was optimized to achieve maximum colour intensity with minimal reagent usage. For this study, the Griess reagent was prepared by dissolving sulphanilamide (50–500 mg), N-(1-naphthyl) ethylenediamine dihydrochloride (NED) (5–50 mg), and 85 % phosphoric acid (1.0–2.0 mL) in 10 mL of ultrapure water. The CNF-MSN composite (0.5 g) was then introduced into 10 mL of the Griess reagent solution and stirred at room temperature for 2 h to ensure effective adsorption of the reagent onto the nanocomposite. The loaded composite was filtered using a vacuum pump and stored in a brown bottle within a desiccator to protect it from light degradation.

2.6. The effect of different operational parameters on the removal efficiency of Cu(ii)

The effect of varying operating conditions on the removal rate of Cu (II) ions using the CNF-MSN composite is defined in the sections below.

The adsorption performance was evaluated by computing the adsorption capacity (Q), and the removal efficiency (%) was calculated using the respective Equations [2]:

$$Qe = \frac{(Co - Ce) \times V}{m}$$

Where Q_e is the adsorption capacity, Co is the initial concentration of analyte, Ce is the final concentration at the equilibrium, V is the volume

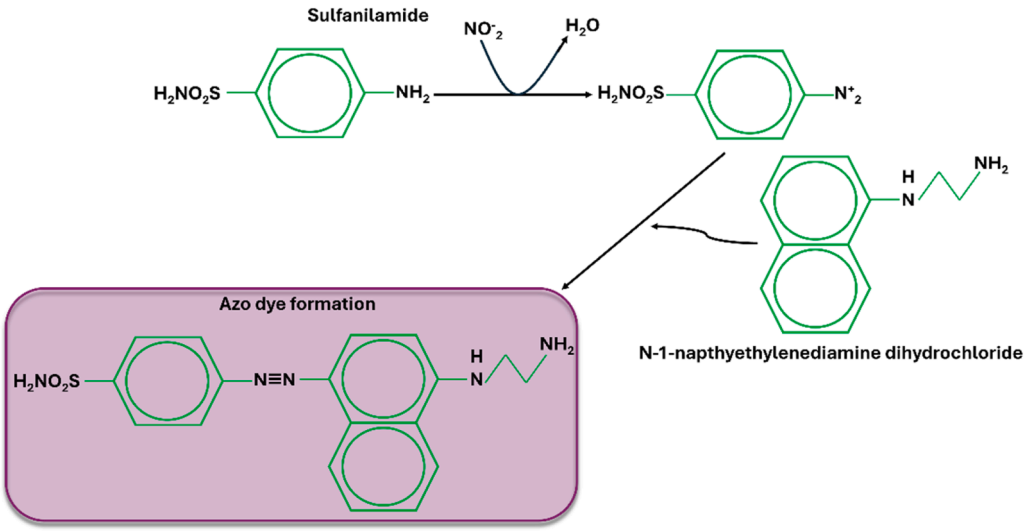

Fig. 3. Reaction mechanism for the formation of Azo dye, N-(1-naphthyl) ethylenediamine (NED), which has a maximum absorbance at 540 nm [35].

of the sample extracted, and *m* is the mass of the adsorbent dosage.

$$R\% = \left(\frac{Co - Ce}{Co}\right) \times 100$$

And where *R %* is the percentage removal efficiency, *Co* is the initial concentration, and *Ce* is the concentration of an analyte at equilibrium.

2.6.1. The effect of initial metal ion concentration

The effect of initial Cu(II) concentration on adsorption efficiency was studied by preparing solutions of varying concentrations: 5.0, 3.0, 1.0, 0.5, 0.1, 0.05, and 0.01 mg/L. Each solution was passed through a solid-phase extraction (SPE) cartridge packed with a fixed amount of CNF-MSN composite under identical experimental conditions conducted in triplicate. The analyte was collected after a fixed contact time of 45 min and analysed for residual Cu(II) content. The results showed that 0.1 mg/L was the optimum initial concentration, yielding the highest removal efficiency, beyond which saturation of active sites limited further uptake.

2.6.2. The effect of adsorbent dosage at a constant time

The effect of adsorbent dosage on Cu(II) ion removal was assessed using SPE techniques, where MSN, CNF, and CNF-MSN composites were packed into SPE cartridges. A 0.1 mg/L Cu(II) solution was passed through the cartridges, allowing a contact time of 45 min to enable sufficient interaction between the metal ions and the adsorbent surfaces. Various adsorbent dosages were tested, ranging from 0.01 g to 0.5 g, in triplicate. The results indicated that 0.5 g was the optimum amount for maximum adsorption efficiency under the given conditions.

2.6.3. The effect of pH

The influence of pH on Cu(II) adsorption was examined over a pH range of 1.0 to 9.0 to prevent metal hydrolysis and ensure accurate adsorption behaviour. Experiments were conducted at room temperature using a Cu(II) concentration of 0.1 mg/L, which is in line with WHO and regional regulatory guidelines (e.g., Economic Partnership Agreement - European Union (EPA-EU)). The pH was adjusted using 0.1 M HCl or NaOH, and adsorption was evaluated through batch experiments with a fixed adsorbent dose conducted in triplicate. The maximum Cu(II) removal was observed at pH 6.20, indicating the optimal pH for adsorption under the given conditions.

2.6.4. The effect of contact time

The effect of contact time on Cu(II) adsorption was investigated using a 0.1 mg/L copper solution passed through SPE cartridges packed with the CNF-MSN composite. The contact time was varied at intervals of 15, 30, 45, 60, and 90 min at room temperature. For each interval, the solution was allowed to pass slowly through the SPE cartridge, and the eluate was collected for analysis after the designated contact time in triplicate. The highest Cu(II) removal efficiency was observed at 45 min, beyond which no significant improvement occurred, indicating equilibrium had been reached. Therefore, 45 min was selected as the optimum contact time and was used for all subsequent adsorption experiments.

2.7. Colorimetric detection procedure

2.7.1. ImageJ analysis (intensity measurements)

An iPhone 8 Plus smartphone was utilized to capture images of the observed color change in quartz cuvettes. The photos were uploaded to an HP laptop for processing utilizing ImageJ (National Institutes of Health, USA, http://imagej.nih.gov./ij) software. The mean intensity (grayscale) of each standard concentration was quantified by delineating a rectangle around each unobstructed area of the cuvette, and the Measure Analysis tool was selected from the ImageJ toolbar. The mean grayscale obtained was further converted to absorbance using the Equation below.

$$A = -\log\left(\frac{I}{Io}\right)$$

Where I is the intensity of light transmitted through the Cu(II) standard, and I_o is the intensity transmitted through a blank (Griess-CNF-MSNs). This was conducted to quantify the amount of Cu(II) in the standards using Beer's Law analysis from a cellphone camera, and to provide the amount of Cu(II) based on the relationship between the colour information and the Cu(II) concentration [36,37]. The analysis was conducted in triplicate ($n = 3$) for statistical purposes.

2.7.2. ImageJ analysis (RGB measurements)

Photograph image of the CNF-MSNs and different Cu(II) concentrations, 0.01–5 mg/L, were analysed using ImageJ software. Initially, the photographed images were processed by eliminating the background light effect to highlight the actual colour of solutions in the cuvettes. This was followed by analysing the histogram of RGB, and the obtained RGB values for each cuvette were recorded. The obtained RGB values were also transferred into the "More fill" colour tab on the MS PowerPoint for further processing. The resultant colour hues were used to produce the rectangular colour patterns and were placed under the photograph image of the obtained colours in the cuvettes. Image

processing was conducted in triplicate to calculate the mean RGB values and standard deviations, which were used to calculate the error bars.

2.7.3. Chromaticity measurements

The attained RGB values were used to calculate the Yxy coordinates using https://colormine.org/convert/rgb-to-yxy. The obtained Yxy values were then used to plot the chromaticity diagrams from the photograph images of the CNF-MSNs and varying Cu(II) concentrations, ranging from 0.01 to 5 mg/L.

2.7.4. XYZ measurements

The obtained RGB values were then utilised to calculate the XYZ values using the equation [38] below, derived from the photograph images of the CNF-MSNs and different Cu(II) concentrations, 0.01–5 mg/L. XYZ measurements were performed in triplicate for mean XYZ values and standard deviation calculation for error bars.

$$X = 0{,}4303\mathrm{R} + 0{,}3416\ G + 0{,}1784\mathrm{B}$$

$$Y = 0{,}2219\mathrm{R} + 0{,}7068\ G + 0{,}071\mathrm{B}$$

$$Z = 0{,}0202\mathrm{R} + 0{,}1296\ G + 0{,}9393\mathrm{B}$$

2.7.5. L*a*b* measurements

The calculated XYZ values were then used to estimate the L*a*b* values using the equation [39] below, derived from the photographs of the CNF-MSNs and different Cu(II) concentrations, ranging from 0.01 to 5 mg/L. L*a*b* measurements were conducted in triplicate for mean L*a*b* values and standard deviation calculation for error bars.

$$\mathrm{L}^* = 116\ (\mathrm{Y}/\mathrm{Y}_0)^{1/3} - 16$$

$$\mathrm{b}^* = 200\ ((\mathrm{Y}/\mathrm{Y}_0)^{1/3} - (\mathrm{Z}/\mathrm{Z}_0)^{1/3})$$

$$\mathrm{a}^* = 500\ ((\mathrm{X}/\mathrm{X}_0)^{1/3} - (\mathrm{Y}/\mathrm{Y}_0)^{1/3})$$

X, Y, Z, *Xo, Yo,* and *Zo* are the coordinates of the CIE XYZ colour space, where *Xo, Yo,* and *Zo* are values of the blank (Griess-CNF-MSNs).

2.7.6. Colour difference (ΔE) measurements

The calculated L*a*b* values were then used to calculate the ΔE values using the equation [40] below of the CNF-MSNs and different Cu (II) concentrations, 0.01–5 mg/L. ΔE measurements were conducted in triplicate for mean ΔE values and standard deviation calculation for error bars.

$$\Delta E = \sqrt{(\Delta L)^2 + (\Delta a)^2 + (\Delta b)^2}$$

2.7.7. Hue angle measurements

Hue angle measurements of the CNF-MSNs and different Cu(II) concentrations, 0.01–5 mg/L were calculated using the equation [40] below. Hue angle measurements were conducted in triplicate for mean hue angle values and the standard deviation calculation for error bars.

$$h = \tan^{-1}\left(\frac{b^*}{a^*}\right)$$

2.7.8. Chroma measurements

Chroma measurements of the CNF-MSNs and varying Cu(II) concentrations, 0.01–5 mg/L, were calculated using Equation [41] below. Chroma measurements were conducted in triplicate to calculate the mean chroma values and standard deviations, which were used to determine the error bars.

$$C^* = \sqrt{(a)^2 + (b)^2}$$

This approach enabled the detection and differentiation of Cu ions through chromatic attributes such as hue and chroma. The methodology applied aligns with the procedures reported by [28] and [42], supporting the reliability and reproducibility of the image-based colorimetric detection strategy.

2.8. Adsorption isotherms and kinetics

To comprehend how adsorbents adsorb heavy metal ions from water, different adsorption isotherm models, namely the Langmuir [43], the Freundlich [44], and the Dubinin-Radushkevich (D-R) [45] models, were employed to understand how metal ions interact with the adsorbent. Each isotherm model has specific constants that describe the surface properties and the extent to which the adsorbent attracts ions. Furthermore, experimental data were analysed using the pseudo-second order model [46] for the optimisation of the process and a better insight into the adsorption mechanism:

The Langmuir model pertains to adsorption, where a monolayer forms on the surface with a finite number of uniformly dispersed sites, as shown in Equation [42] below.

$$\frac{C_{eq}}{q_{eq}} = \frac{1}{Kq_{max}} + \frac{C_{eq}}{q_{max}}$$

Where C_{eq} is the equilibrium concentration in the solution, q_{eq} is the amount of Cu(II) ions adsorbed when equilibrium is reached, K is the adsorption equilibrium constant, and q_{max} is the maximum adsorption capacity. Plotting C_{eq}/q_{eq} against C_{eq} yields a straight line with a slope of $1/q_{max}$ and an intercept of $1/Kq_{max}$.

The Freundlich model, which characterizes adsorption on a heterogeneous surface, addresses non-identical and/or non-uniform binding sites, as shown in Equation [43].

$$lnq_{eq} = lnK_F + \frac{1}{n} lnC_{eq}$$

Where K_F represents the adsorption capacity, and n indicates the adsorption intensity. Plotting lnq_{eq} against $\ln C_{eq}$ helps determine K_F and $1/n$.

The pseudo-second-order model was employed to investigate the adsorption of Cu(II) ions onto the CNF-MSN composite, as described by Equation [45] below.

$$q_t q_3 - \left(\frac{1}{q_e} + k_2 t\right)^{-1}$$

Where q_e and q_t (mg/g) are the adsorption capacity at equilibrium and at time t (min), and k_2 (g/mg min) is the pseudo-second order rate constant.

3. Results and discussion

3.1. Transmission electron microscope (TEM) and scanning electron microscope (SEM) analysis

The TEM micrographs of cellulose nanofibers (CNF) are shown in Fig. 4a and b, extracted from wood pulp, while the SEM micrographs are depicted in Fig. 4c and d. From the TEM analysis, a distinctive web-like structure depicting nanofibers was observed (Fig. 4a), with an average diameter of ~33 nm (Fig. 4b). The CNF web-like structure suggests an interconnected and intricate network of nanofibers because of defibrillation. The SEM images showed the typical characteristics of mesoporous silica nanoparticles, confirmed by their spherical shape (Fig. 4c and d). The average particle size of MSN ranges from 2 to 50 nm (Fig. 4e), and the particles were relatively uniform. According to Dhaneswara et al., the type of silica produced in this study is referred to as heterogeneous mesoporous silica [47]. The brighter surfaces represent amorphous silica, while the darker surfaces indicate the pore cavities [47].

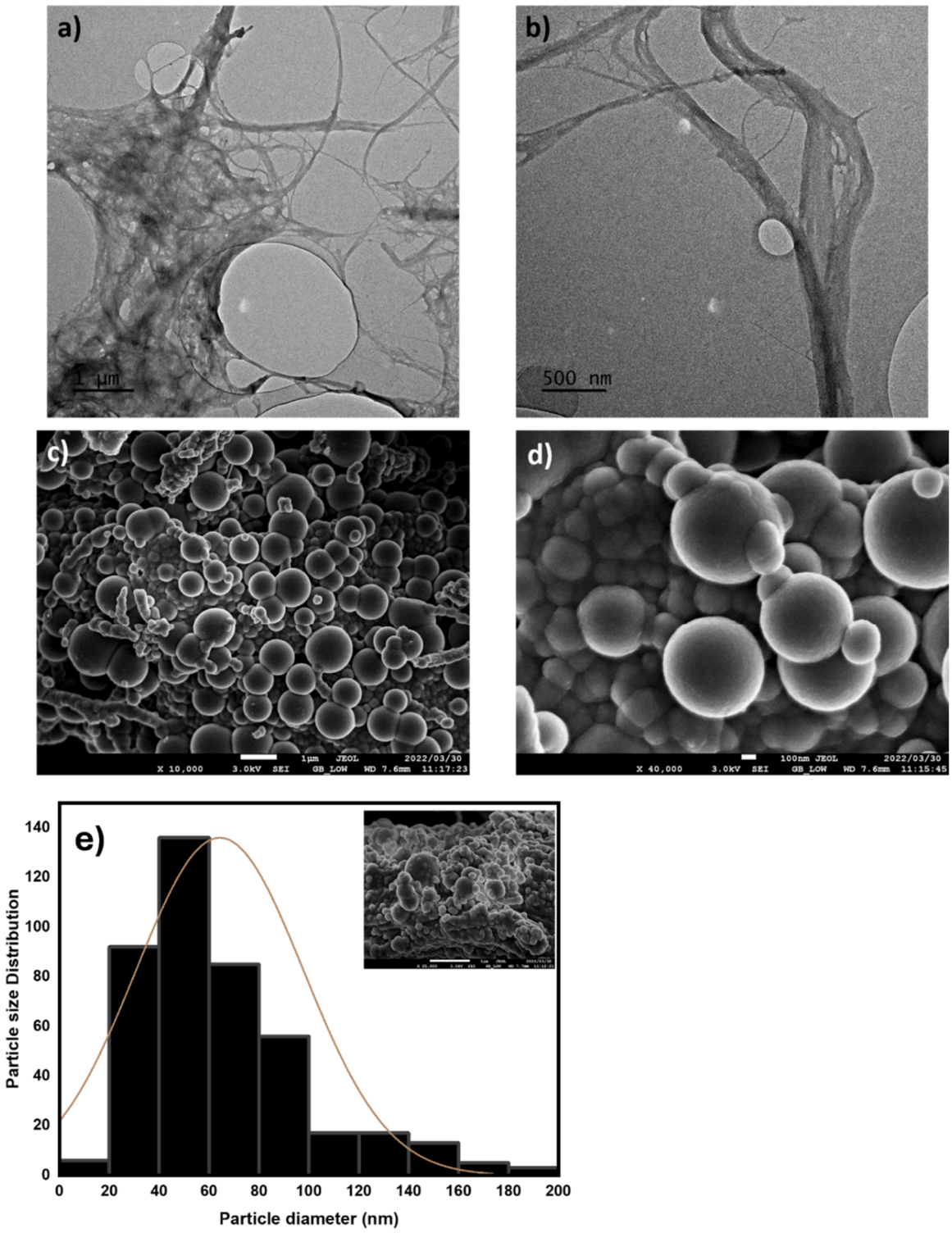

Fig. 4. TEM micrographs of CNF (a and b), SEM microscopy of MSN (c and d), and particle side distribution of MSN (e).

3.2. Attenuated total reflection Fourier transform infrared (ATR-FTIR) analysis

The ATR-FTIR analysis was used to identify the functional groups associated with CNF, MSN, and CNF-MSN composite. Fig. 5 shows the CNF spectrum, which exhibits a broad band at ~3330 cm^{-1}, attributed to the O—H stretching vibration of the hydroxyl group in cellulose, as confirmed by a hydrogen bonding peak between 1600 and 1650 cm^{-1}. A peak at ~2900 cm^{-1} due to the C—H aliphatic axial deformation of CH_2/CH_3 is also observed. Two peaks observed at ~1050–1150 cm^{-1} and 897 cm^{-1} indicated the C–O stretching and C—H deformation of cellulose [48], confirming β-glycosidic linkages in cellulose [48,49]. For MSN, the structure was confirmed by typical firm peaks at ~1100 cm^{-1} and 800 cm^{-1}, attributed to the asymmetric and symmetric stretching of the Si-O-Si group, respectively [50]. Further peaks were observed at ~450–500 cm^{-1}, associated with the Si-O bending vibrations, and a weak peak at ~803 cm^{-1}, indicating surface silanol groups (Si–OH) [51], due to unreacted TEOS. The CNF-MSN composite spectrum

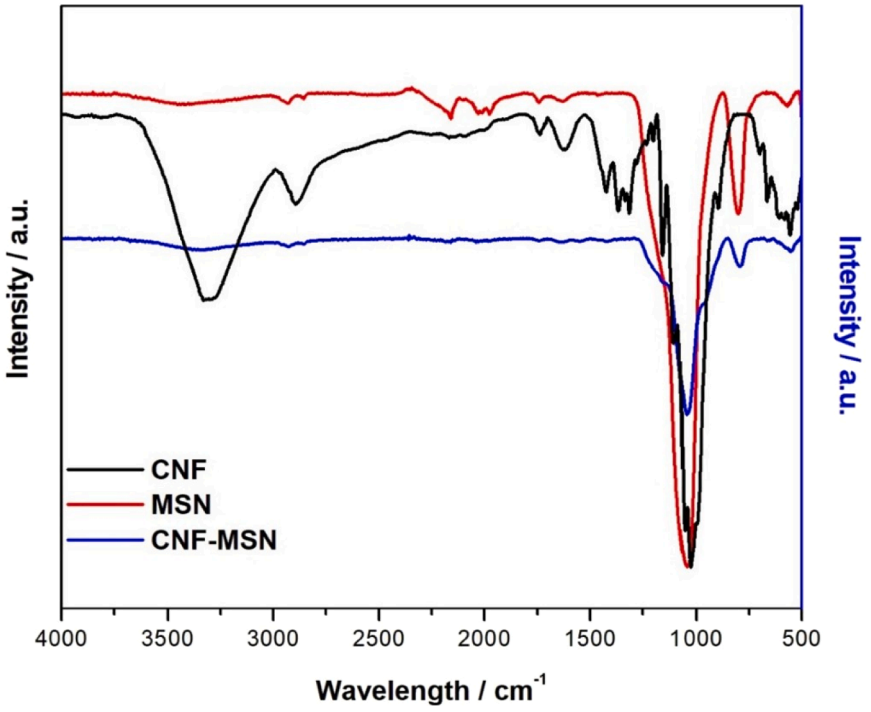

Fig. 5. FTIR Spectra of CNF, MSN, and CNF-MSN composite.

exhibited combined features of CNF and MSN, with notable shifts or changes that confirmed the interaction of the materials, as indicated by the weak O–H stretching, suggesting hydrogen bonding between the hydroxyl groups in CNF and the surface silanol groups of MSN. The Si-O-Si peaks remain visible, albeit with reduced intensity, due to their incorporation into the cellulose matrix. On the other hand, the C—O-C and C—H bands from CNF are still present, confirming that the organic structure remains intact. Shifts or changes in peak intensity around 1000–1100 cm^{-1} indicate chemical interactions or physical mixing of the two-phase components, which suggests a successful fabrication of the composite.

3.3. X-ray diffraction (XRD) analysis

The XRD diffractograms of CNF, MSN, and CNF-MSN composite are shown in Fig. 6, where the CNF shows a sharp peak at $2\theta = 15^{\circ}$ and $2\theta =$

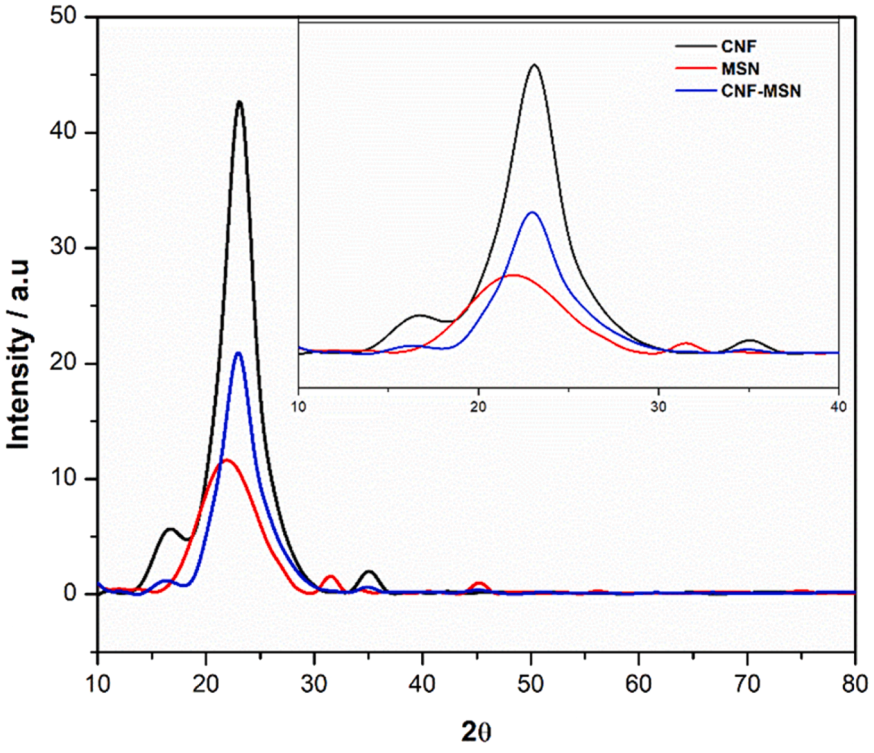

Fig. 6. X-ray diffractograms of CNF, MSN, and CNF-MSN composite.

22°, corresponding to the crystallographic planes (101) and (002) associated with the amorphous and crystalline structure of cellulose, respectively. The XRD patterns for MSN exhibit a broad hump and a distinct peak, typically located around 2θ = 22–24°, characteristic of amorphous silica materials. The peak aligns with a previous study on mesoporous silica nanoparticles [49,51]. The incorporation of silica into cellulose significantly diminished its crystallinity by disrupting the orderly chain structure, as indicated by the CNF-MSN peak at 2θ = 22°. Similar results were reported by Mazibuko et al. (2024) for amine-functionalized cellulose-silica composites used in the remediation of hexavalent chromium (Cr(IV)) in contaminated water [52]. The incorporation of amorphous silica disrupts the orderly alignment of cellulose chains, decreasing overall crystallinity, as confirmed in Table 1.

3.3. Thermogravimetric analysis (TGA) analysis

The TGA and differential thermogravimetric (DTG) curves for CNF, MSN, and CNF-MSN composite are depicted in Fig. 7a and b, respectively. The thermal degradation steps of CNF and CNF-MSN composite show similar decomposition patterns at 100 °C, 250 °C, and 350 °C due to evaporation of absorbed moisture and the degradation of the cellulose main chain, respectively. On the other hand, the inclusion of MSN in CNF significantly decreased the thermal stability of cellulose (CNF-MSN) (Fig. 7b), which can be attributed to poor interaction between the cellulose and silica nanoparticles. In normal circumstances, the incorporation of metal oxides in composite materials tends to improve the thermal stability of the composite due to their ability to form a barrier network and char formation, which hinders the transfer of volatile products during heating. In this case, due to poor interaction, the nanoparticles accelerated the degradation of cellulose. At the same time, at high temperatures, an increase in thermal stability was observed due to char formation, which delayed the degradation of CNF-MSN. Large amounts of char (80 %) were observed (Fig. 7a). As anticipated, MSN remained stable at baseline within 900 °C.

3.4. Brunauer-Emmett-Teller (BET) analysis

The BET analysis provides crucial insights into the surface properties and porosity, which are essential for understanding the adsorption capabilities of the investigated materials. The synthesised materials exhibit Type IV isotherms, typical for mesoporous materials (Fig. 8a), with an average pore diameter ranging from 2 to 50 nm (Fig. 8b), confirming that the porosity is composed of mesopores. This classification aligns with the characteristics of mesoporous materials [51,53–55]. CNF shows the highest nitrogen uptake, indicating the availability of accessible pores. This is followed by MSN with moderate adsorption, showing characteristics of mesoporous silica. In contrast, the CNF-MSN composite exhibits the lowest adsorption, indicating that the combination of CNF and MSN results in a lower accessible surface area. This may be attributed to reduced nitrogen accessibility, pore blocking, or structural rearrangements during the synthesis of the composite. Furthermore, pore size distribution derived from desorption indicates that CNF has a narrow mesopore distribution ~3 nm, and MSN shows a broader mesoporous profile ~ 6–10 nm. In comparison, CNF-MSN exhibits a broad and shifted distribution toward macropores (>50 nm), suggesting agglomeration during synthesis and pore expansion formation. Table 2 also indicates the observed behaviour of CNF (3.529 m^2/g), MSN (5.777 m^2/g), and CNF-MSN (14.77 m^2/g), with a significant shift in the average pore diameter of 68.19 nm, respectively. These findings support the results obtained through nitrogen sorption, where the synthesized xerogels were found to be type IV silica with a mesoporous structure [51].

Table 1
Summary of particle size and crystallinity index determined from XRD.

Samples	Particle size/nm	CI %
CNF	22.3	47.1
MSN	–	–
CNF-MSN	20.5	37.8

3.5. Optimisation of loading volume for colorimetric detection

To determine the optimum loading volume for the colorimetric reaction, varying volume ratios of the blank (Griess-CNF-MSN) and 0.01 mg/L Cu(II) solution were evaluated. The tested volume ratios (μL) included 900:100, 800:200, 700:300, 600:400, 500:500, (Griess-CNF-MSN:Cu(II)) solution. The 600:400 μL ratio produced the most distinct and intense colour change among these. It produced the highest absorbance at a wavelength of 520/540 nm, as shown in the bar graph in Fig. 9, indicating the optimal volume ratio for effective colorpment and sensor performance. The optimised volume ratio of 600:400 μL was subsequently employed to analyze varying Cu(II) concentrations ranging from 0.01 to 5 mg/L. This ratio was selected based on its ability to produce the most pronounced colour response, ensuring consistent and reliable results across the tested concentration range.

The photograph of Cu(II) concentration ranging from 0.01 to 5 mg/L (from right to left), including a blank (Griess-CNF-MSN), as shown in Fig. 10a, depicts an apparent colour change from pale pink to deep purple as the concentration of copper ions increases. Fig. 10b also revealed that the red and blue curves followed a similar pattern, indicating a colour transition to the green region with increasing Cu(II) concentration. The colour transition implies the aggregation of the Griess reagent composite in the presence of Cu(II) ions or the binding of Cu(II) ions onto the composite. Similar observations were reported on the colorimetric assay for Cu(II) using a multiple antibiotic resistance regulator (MarR) [56,57], where in the presence of Cu(II), the Griess reagent composite aggregated with a change in colour from pale pink to deep purple, visually by the naked eye, as the copper concentration increased. In addition, due to aggregation, the intensity of the surface plasmon resonance band at 540 nm decreased, and a new peak appeared at 520 nm from 1 to 5 mg/L. Furthermore, the obtained RGB values, as shown in Fig. 10b, were utilized to get the More Fill colour patterns, as shown in Fig. 10a (below the cuvettes). This was achieved by filling in the RGB values for each standard, which resulted in colours corresponding to those depicted in each cuvette. The observed colours validated the efficiency of the ImageJ approach. Subsequent chromaticity analysis was carried out using the CIE system, as shown in Fig. 10c. This approach involved defining the three standard primary colors X, Y, and Z, which can be combined to form all perceivable colors, also known as imaginary colors. The CIE Yxy diagram in Fig. 10c, which has a horseshoe shape, confirms the aggregation of Griess reagent composite, evidenced by a visible shift from the pink region typical of dispersed nanoparticles towards a purple shade upon aggregation. The results from the chromaticity diagram corresponded with the colour changes observed by the naked eye. Moreover, the apparent colour changes agreed with the region in the chromaticity diagram, further validating the novel ImageJ approach for detecting Cu(II) using CNF-MSNs and a Griess reagent. At varying concentration levels, the red and blue components of the colour model aligned almost parallel to one another, producing a range of deep purple shades [58]. These variations were influenced by the intensity of the solution, which played a crucial role in accurate colour determination.

The XYZ values shown in Fig. 11a did not show any notable trend. However, the depicted trend for the three variables corresponded to the RGB values in Fig. 11b Thus, this validates the efficiency of the ImageJ approach. Further studies were conducted to investigate the behaviour of the L*a*b* values, and the obtained results are illustrated in Fig. 11b The L* curve exhibited a similar trend to the G curve (Fig. 10b), indicating a shift in the standards from lighter to darker shades, reflected by the decreasing L* values. Meanwhile, a significant increase was

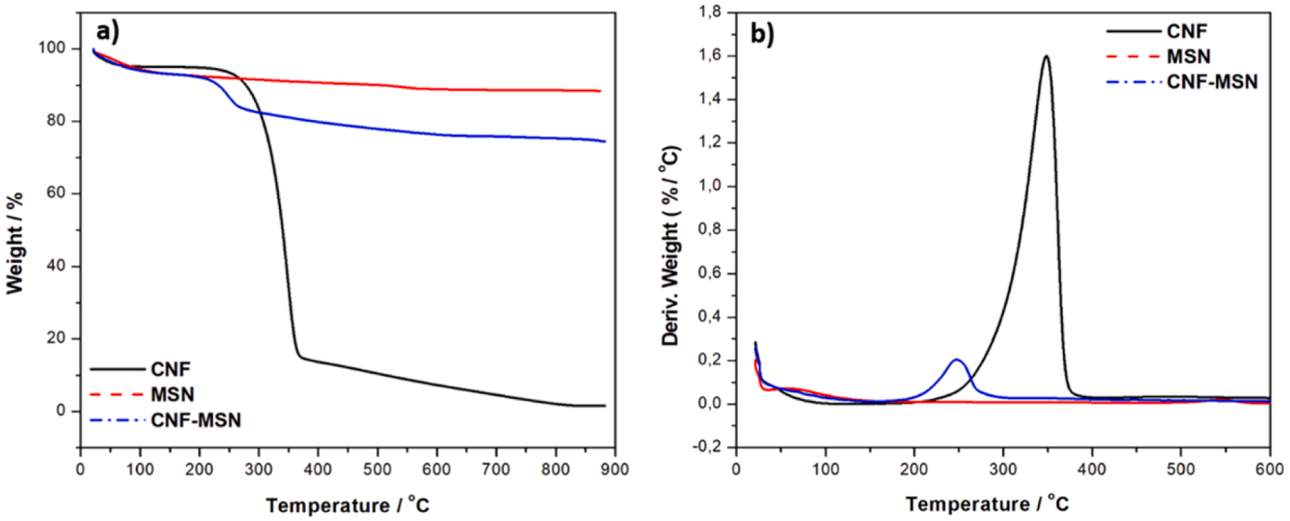

Fig. 7. (a) TGA and (b) DTG curves of CNF, MSN, and CNF-MSN composite.

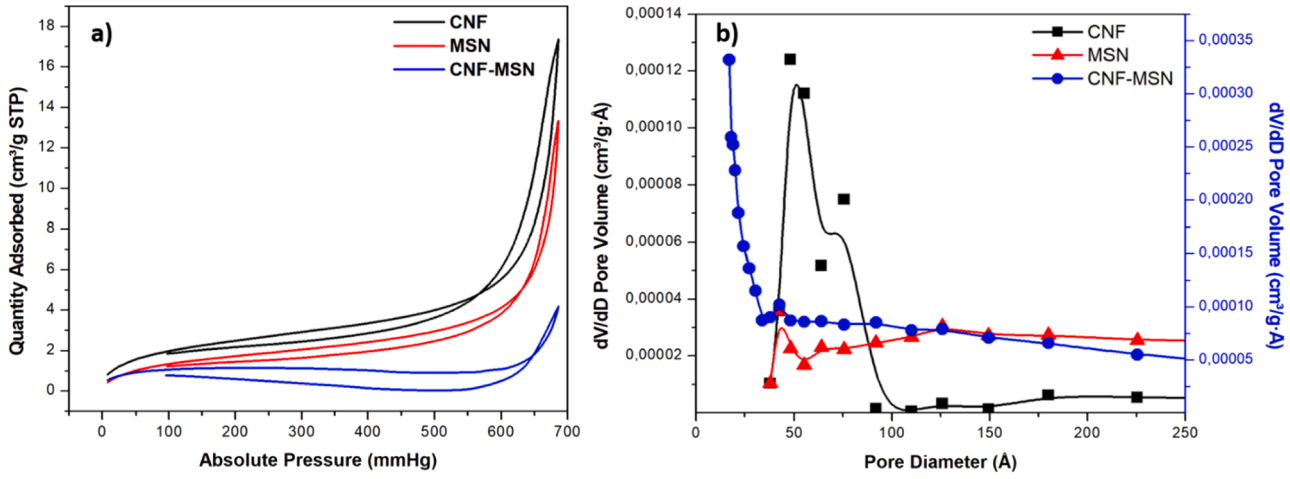

Fig. 8. Nitrogen adsorption–desorption isotherms, (a) pore size distribution and (b) pore diameter for MSN, CNF, and CNF-MSN.

Table 2
Summary of BET surface analysis.

Sample	Surface area m^2/g	Average pore size nm	Pore volume cm^3/g
CNF	3.529	3.29	0.002961
MSN	5.777	6.79	0.009810
CNF-MSN	14.77	68.19	0.02911

observed in the a* curve from 0.5 to 5 mg/L, with the a* values increasing from hostile to positive values (moving from green to red), corresponding to the observed colour changes from pale pink to dark purple. A rapid increase in the b* values was observed from the blank to 0.5 mg/L (increase from -b* to $+b^*$), followed by a rapid decrease from $+b^*$ to -b* from 0.5–1 mg/L, corresponding to the significant colour change from pale pink to dark purple.

A rapid increase in the colour difference was noted as the Cu(II) concentration increased from blank to 0.5 mg/L, followed by a significant decrease from 0.5 to 1 mg/L due to the intense colour change from light pink to dark purple, as depicted in Fig. 12(a). This was followed by another rapid increase from 1 to 5 mg/L of Cu(II). The observed results suggested that the ΔE values increased proportionally with increasing Cu(II) concentrations, indicating a positive correlation between colour change and analyte concentration. A significant decrease in hue was observed as the Cu(II) concentration increased from the blank (1 mg/L), indicating a shift from the red to the blue region in Fig. 12b (red line). These results corresponded to the perceived colour change from light pink to dark purple. Subsequently, a significant increase was noted from 1–3 mg/L, followed by a decrease at 5 mg/L (Fig. 12b, blue line). A rapid rise in chroma was observed from the blank to 0.5 mg/L, followed by a rapid decrease from 0.5 to 5 mg/L. The decline in chroma values indicated a shift in the colour response from vivid to more subdued tones, reflecting a reduction in colour intensity as chromaticity decreased.

The sensitivity of the synthesised CNF-MSN composite in the presence of the Griess reagent to Cu(II) was investigated by the addition of 400 μL of varying concentrations of Cu(II) standards in the range of 0.01–5 mg/L to 600 μL of Griess-CNF-MSN. The intensity of each standard was measured, corrected, and converted to absorbance using Equation 2.3. A calibration plot was created, yielding a linear correlation between the absorbance and concentration of Cu(II) in a range of 0.01–5 mg/L, as shown in Fig. 13. Based on the lowest standard concentration of 0.01 mg/L, the ImageJ method's limit of detection (LOD) was found to be 0.001521 mg/L. The analysis was performed in triplicate, a standard deviation was calculated, a slope was taken from the calibration plot, and the LOD was calculated as follows: $LOD = 3 \times SD/M$, where SD: standard deviation and M: the slope of the calibration graph.

The Griess-CNF-MSN solution colour changed from pale pink to dark

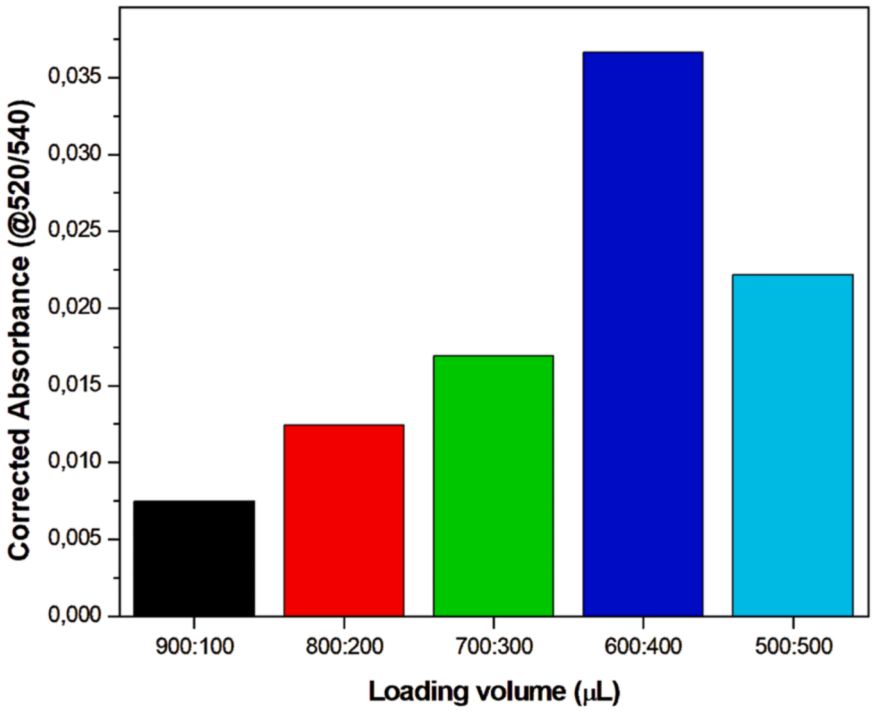

Fig. 9. Bar graph of absorbance at 520/540 nm vs loading volume (μL).

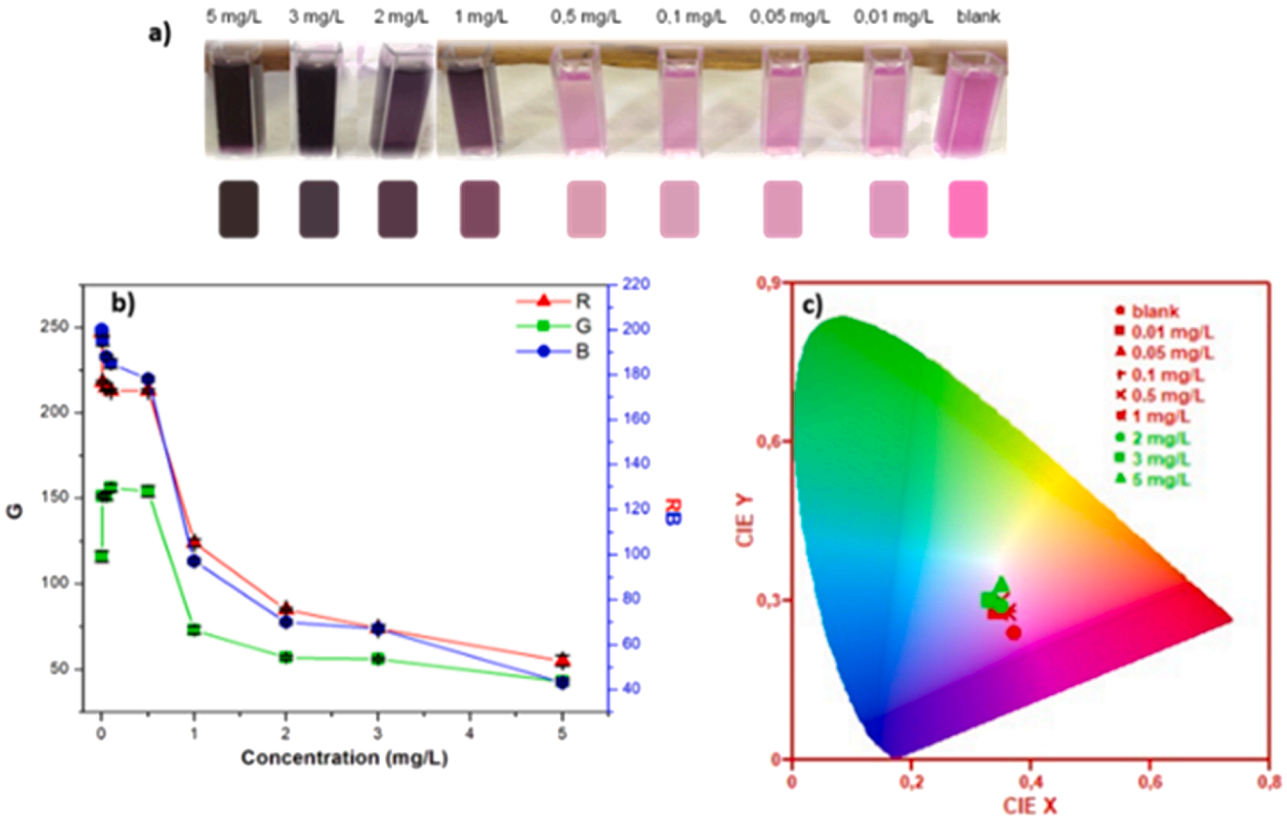

Fig. 10. (a) Photographed picture of Griess-CNF-MSNs and different concentrations of Cu(II) in the range of 0.01– 5 mg/L, (b) Illustration of the R, G, and B colour combination dynamics for the corresponding Cu(II) concentration and (c) chromaticity diagram of Griess-CNF-MSN and Cu(II) standards 0.01–5 mg/L.

purple with increasing Cu(II) concentration from 1–5 mg/L, as observed in Fig. 14a, with an absorption peak at 540 nm as depicted in Fig. 14a. A significant decrease in the absorption peak at 520 nm was noted as Cu (II) concentration increased, resulting in a new absorption peak at 520 nm. The absorbance at 520/540 nm was calculated. A calibration plot was constructed, yielding a linear correlation between the absorbance at 520/540 nm and the concentration of Cu(II) in a range of 0.01–5 mg/L (Fig. 14b). The limit of detection was 0.006253 mg/L, calculated using

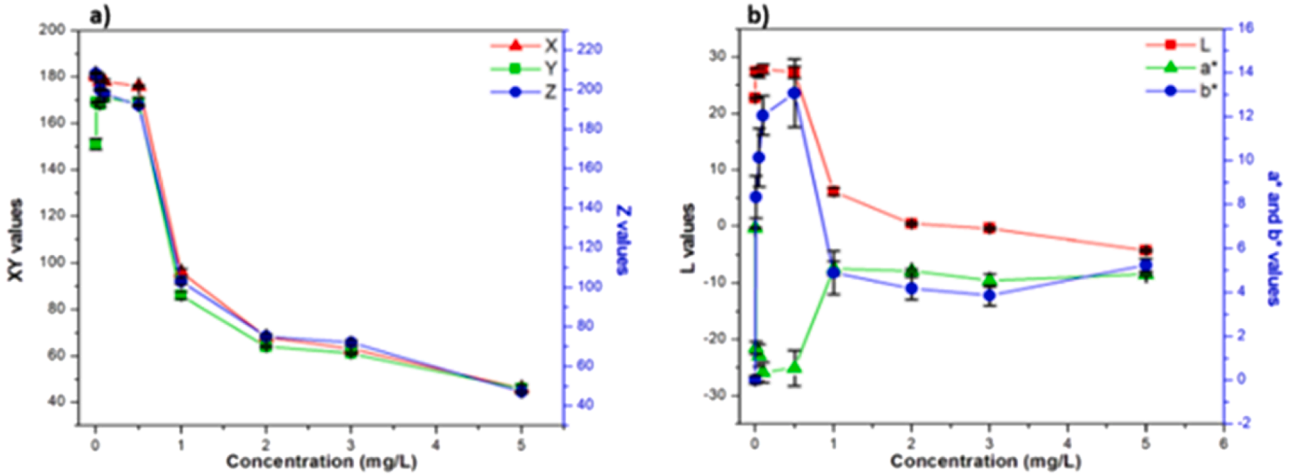

Fig. 11. (a) Plots of XY values vs concentration, and (b) L*a*b* values against concentration.

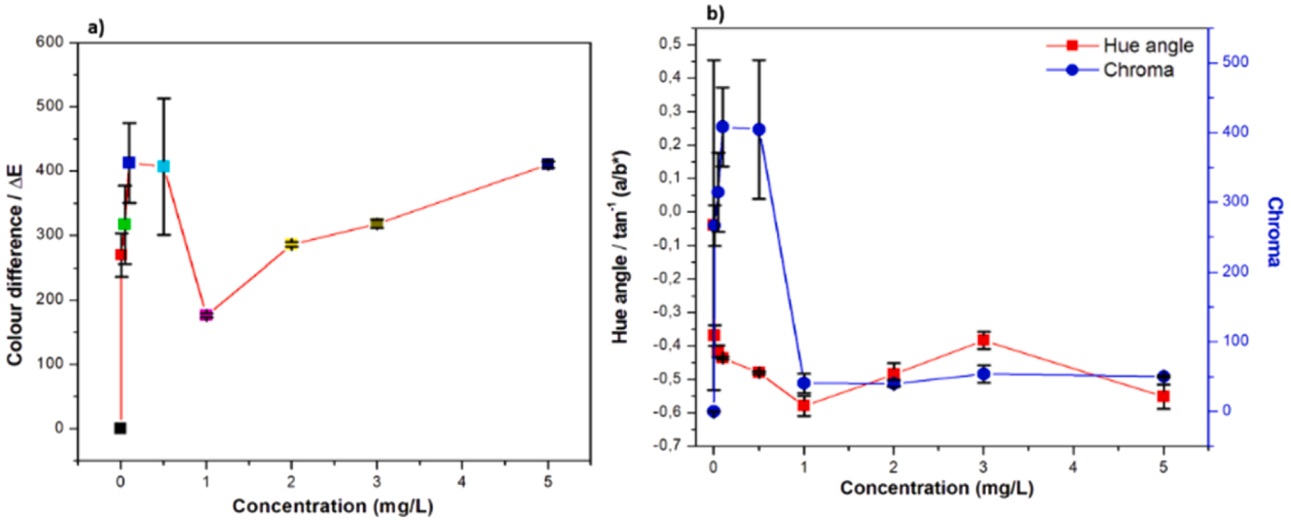

Fig. 12. (a) Plot of colour difference against concentration and (b) plots of chroma and hue angle vs concentration.

the lowest standard of 0.01 mg/L. The analysis was conducted in triplicate, a standard deviation was calculated, a slope was taken from the calibration plot, and the LOD was calculated as follows: LOD = 3×SD/M, where SD is the standard deviation. M is the slope of the calibration graph.

The synthesized colorimetric sensor demonstrated the detection operation and feasibility of a low detection limit. This method proved to be inexpensive, rapid, and sensitive to Cu(II) ions at optimum experimental conditions, compared to other traditional methods [59,60].

3.6. Adsorption isotherms and kinetics

The effect of different operational parameters on the removal efficiency of Cu(II) ions using CNF-MSN composite is shown in Fig. 15a-d. For the effect of initial Cu (II) concentration, it is observed that as the initial Cu (II) concentration increased from 0.01 to 5.0 mg/L, a gradual decrease in removal efficiency (85–40 %) was observed (Fig. 15a). This decline suggests saturation of the available active adsorption pore sites at higher metal ion concentrations [9,61]. Despite this, the optimum removal efficiency (~90 %) at 0.1 mg/L was observed, demonstrating the composite's efficiency in removing Cu(II) ions up to concentrations of 0.3 mg/L. The effect of adsorbent dosage results showed that increasing the dosages of CNF-MSN increases the removal efficiency (~0.9–80 %) of Cu(II), with a maximum at 0.5 g (Fig. 15b). This demonstrates that greater amounts of adsorbent provide more active binding sites, enhancing removal efficiency. It can be stated that the higher Cu (II) concentration brings a driving force to defeat the mass transfer obstacle in the aqueous phase and at the surface of the solid material [51,54,62]. The effect of pH significantly influenced the removal efficiency (~85 %), with optimum adsorption occurring at pH 6.20 (Fig. 15c). This implies that removal at pH 6 is due to favourable electrostatic interactions between Cu(II) species and the adsorbent surface [63,64]. The effect of contact time was also investigated; the Cu(II) removal efficiency increased with contact time, reaching equilibrium at approximately 45 min, as shown in Fig. 15d However, it also demonstrated high removal efficiency after 45 min. This indicates sufficient interaction between the adsorbent and Cu(II), resulting in more effective adsorption. Similar adsorption behaviour is reported in other literature [13,65–68], where rapid adsorption was reported due to the availability of active sites to form complexes on the adsorbent surface. On the contrary, the slow adsorption was observed because the active sites of the adsorbent were limited, and the gradual sorption process eventually reached equilibrium. Hence, for real samples, these optimum conditions — 0.1 mg/L, pH 6.20, dosage 0.5 g, and 45 min contact time — were further used for Cu(II) removal in tap water, deionized water, and wastewater.

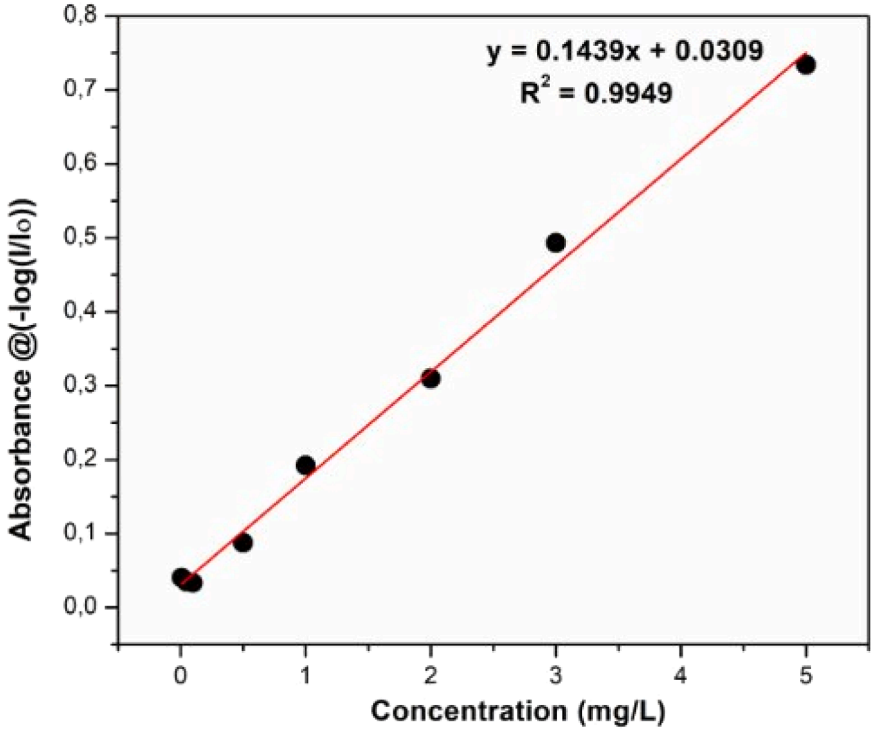

Fig. 13. Calibration plot of corrected absorbance vs different Cu(II) concentrations, 0.01–5 mg/L.

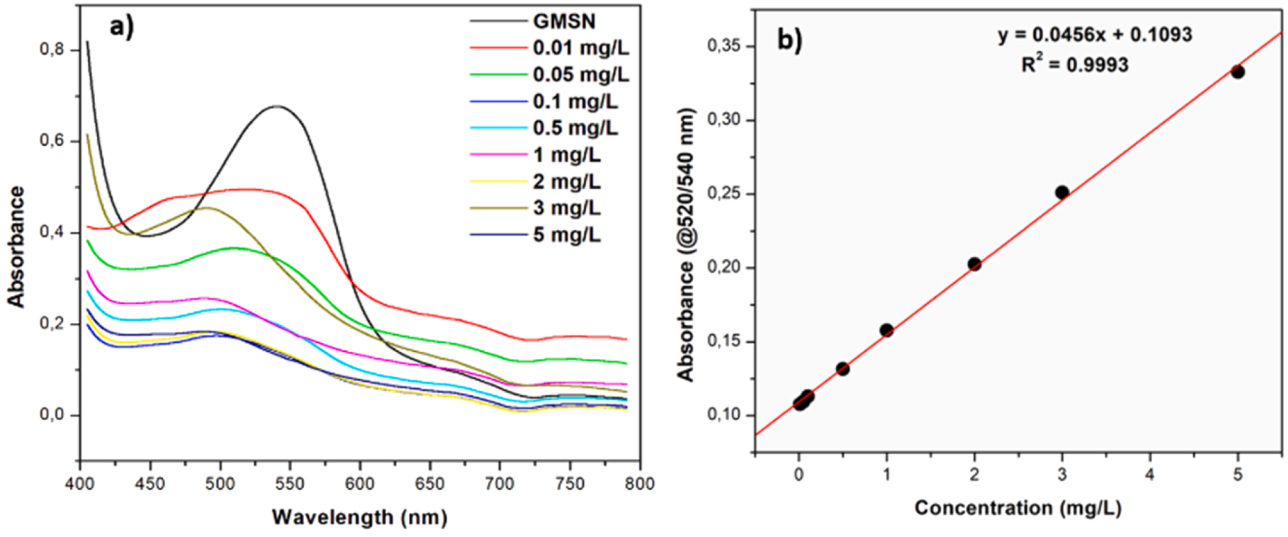

Fig. 14. (a) The UV/visible spectra of different concentrations, and (b) the Calibration curve of 0.01 mg/L-0.5 mg/L, at 540/520 nm wavelength.

Table 3 outlines the results of the adsorption of copper by CNF, MSN, and CNF-MSN. CNF-MSN exhibited the highest adsorption capacity of 97.8 mg/g and a higher metal removal efficiency of 97.9 % compared to CNF and MSN. The high surface area and active functional groups (like hydroxyl and carboxyl) on CNF provided a more active site for the adsorption of copper ions. This suggests its potential as a bio-based adsorbent for copper removal from aqueous solutions. Conversely, MSN demonstrated an adsorption capacity of 92.2 mg/g and a metal removal efficiency of 92.2 %. CNF showed the lowest adsorption capacity (19 mg/g) and metal removal efficiency (1.9 %). These results correlate with BET analysis, which suggests that the adsorbents with a high surface area tend to have high adsorption capacity. These results indicate that MSN and CNF have limited availability of active adsorption sites for copper ions compared to CNF-MSN. CNF-MSN outperformed both individual components, achieving an adsorption capacity of 97.8 mg/g and a metal removal efficiency of 97.9 % (Table 3).

This suggests a significant interaction effect between CNF and MSN, resulting in increased surface area, pore size, and pore volume, as confirmed by BET analysis. The composite exhibited the properties of both materials, such as MSN's high surface area and CNF's functional groups, thereby enhancing the adsorption properties, due to the availability of active sites and large surface area for the adsorption of copper ions. Furthermore, the CNF-MSN composite application in different water samples, including tap water, deionized water, and wastewater, demonstrated effective and efficient removal of copper ions, achieving a removal efficiency ranging from 95 to 99 % and a high adsorption capacity of 37.5–39.8 mg/g (Table 4).

The adsorption of Cu(II) ions onto the CNF-MSN composite was

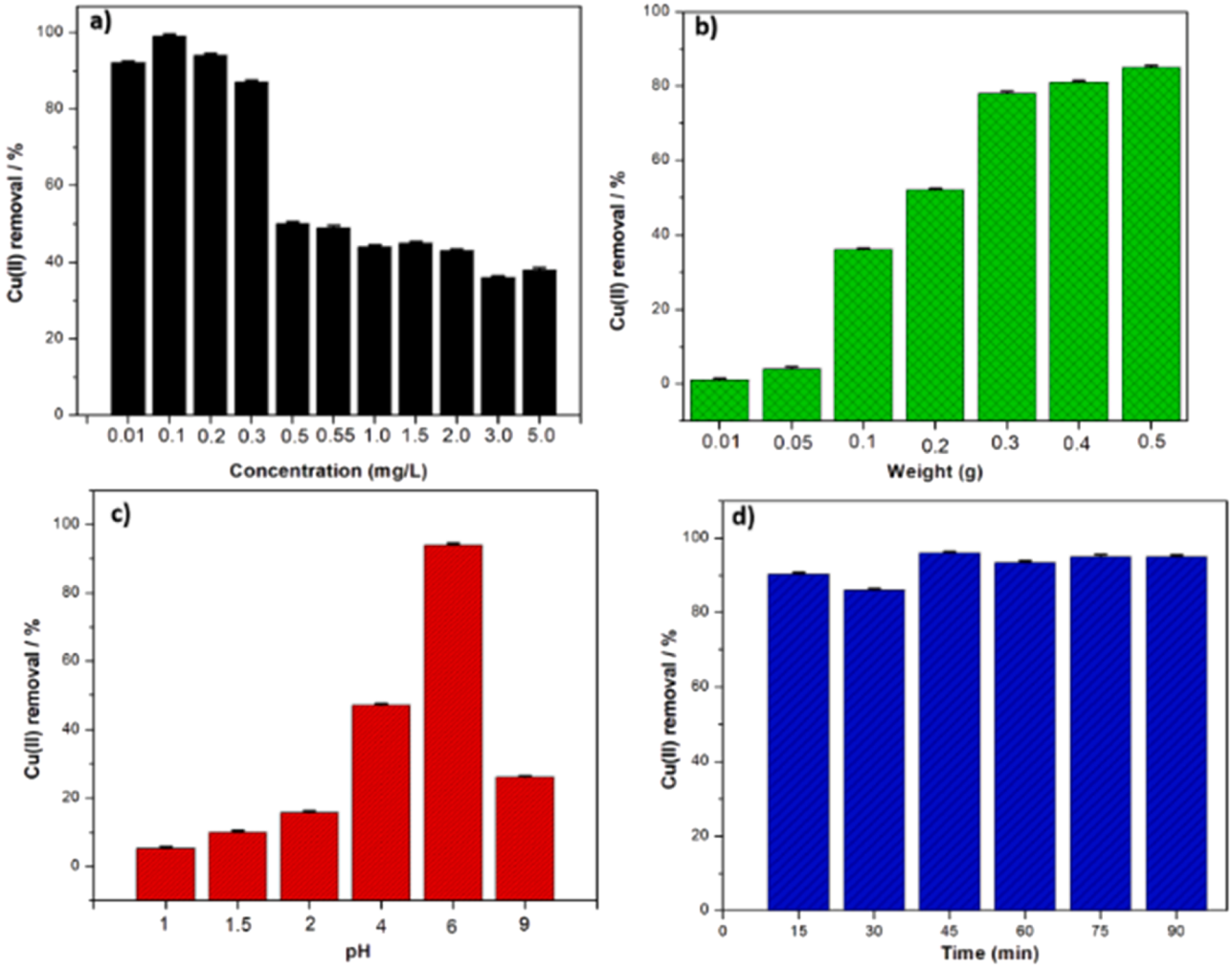

Fig. 15. Effect of varying operating conditions on the Cu(II) removal percentage: (a) initial concentration, (b) adsorbent dose, (c) pH, and (d) contact time.

Table 3
Adsorption of copper by different types of materials.

Samples	Adsorption capacity (mg/g)	%Removal efficiency
CNF	19	1.9
MSN	92.2	92.2
CNF-MSN	97.8	97.9

Table 4
Adsorption of copper using an effective material type, CNF-MSN, on wastewater, tap water, and deionised water.

Samples	Removal efficiency (%)	Adsorption capacity (mg/g)
Wastewater	99.1	39.8
Tap water	94.5	37.5
Deionised water	98.1	39.6

evaluated using Langmuir, Freundlich, and Dubinin-Radushkevich (D-R) isotherm models, and the pseudo-second order (PSO) model results are depicted in Fig. 15a-d and summarised in Table 3. For the Langmuir model, the data showed a poor fit with the model having a value of $R^2 = 0.546$, indicating poor adsorption for a monolayer on a homogeneous adsorbent surface (Fig. 16a). A moderate fit $R^2 = 0.8852$ was observed for the Freundlich model, which suggests that the adsorption of Cu(II) postulates a heterogeneous adsorption process occurring on a multi-layer CNF-MSN surface (Fig. 16b). Similar findings were reported by Hemdan et al., in activated carbon thin film-zeolitic imidazolate framework-8 (ACTF@ZIF-8) nanocomposite for efficient methylene blue removal [65]. This implies that the elevated R^2 value signifies that the Freundlich model accurately represents the complexity of the adsorption process, suggesting the involvement of multiple types of binding sites on the composite material [14,65,69,70]. On the other hand, the highest value of $R^2 = 0.9795$ and a better fit were observed for the D-R isotherm, which suggests that the adsorption mechanism is pore-filling rather than surface binding and energetically heterogeneous (Fig. 16c). This implies that the porous nature of MSN in the CNF-MSN composite influenced the adsorption via the pores of the mesoporous silica, while CNF influenced multi-layer adsorption. This means that the adsorption mechanism for CNF involves multilayer adsorption on a heterogeneous surface. At the same time, CNF-MSN followed pore-filling and heterogeneous, accompanied by chemisorption, as indicated by the kinetic studies, which suggest that the primary mechanism followed the pseudo-second-order model, $R^2 = 0.9994$ (Fig. 16d). Mazibuko et al. conducted a similar analysis for the adsorption of hexavalent chromium Cr(VI), using amine-functionalized cellulose-silica composites [52]. Their findings showed that the composite's adsorption behaviour towards Cr(VI) exhibited a higher regression coefficient for the PSO kinetic parameter [52]. The adsorption of Cu(II) ions by CNF-MSN is influenced by several factors, including surface area, pore volume, active sites, reduced crystallinity, adsorbate-adsorbent interaction, and time dependence, which follow the PSO model.

Table 5

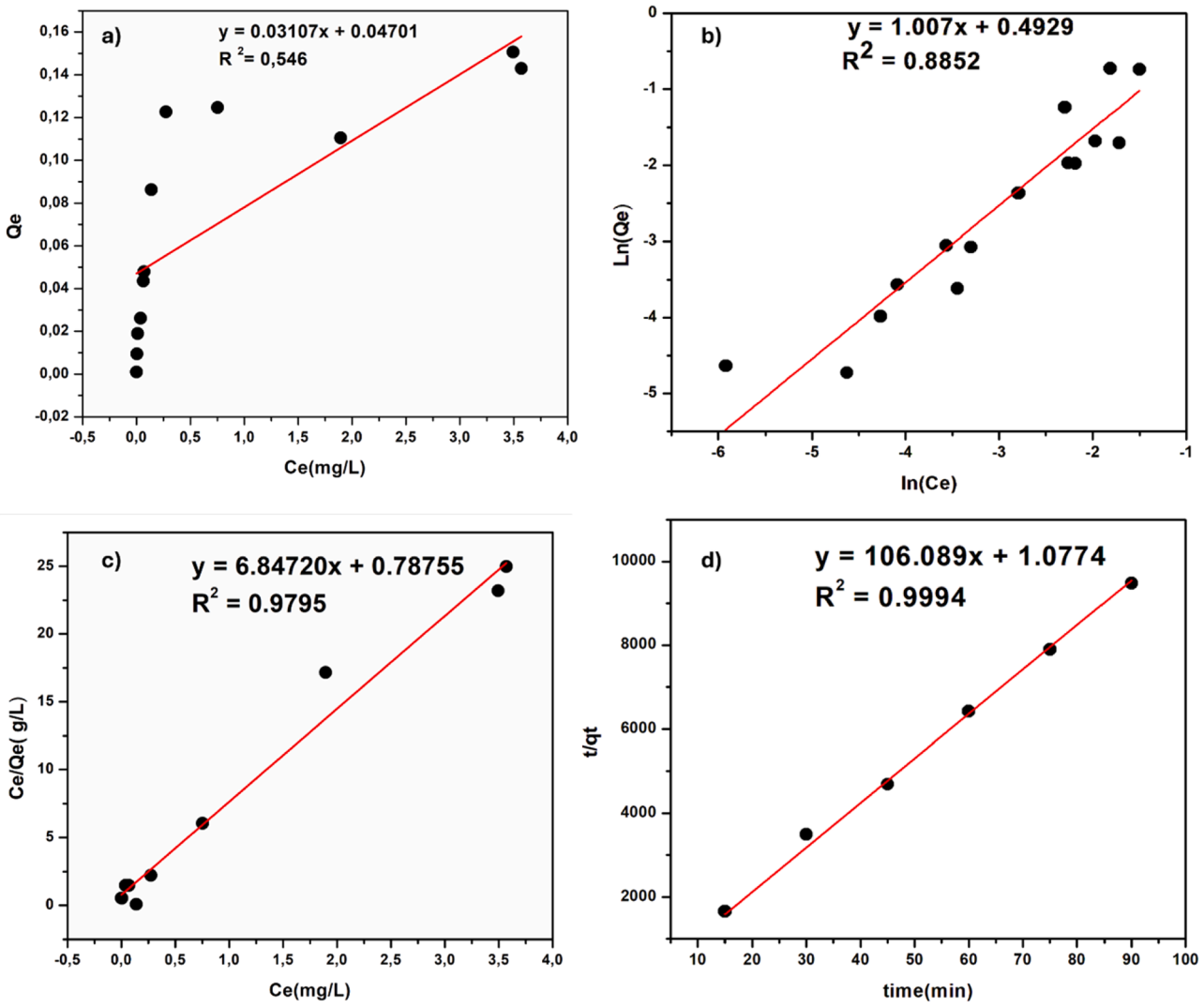

Fig. 16. (a) Langmuir isotherm, b) Freundlich (linear), (c) Dubinin-Radushkevich (D-R) adsorption isotherms, and d) PSO linear plot for CNF-MSN composite.

Table 5
Summary of linear fits.

Isotherm model	R^2 value	Fit quality	Adsorption type
Langmuir	0.546	Poor	Monolayer (not suitable)
Freundlich	0.885	Good	Multilayer on a heterogeneous surface
D-R	0.980	Excellent	Chemisorption

Conclusion

This study demonstrated that a novel cellulose nanofiber-mesoporous silica nanoparticle (CNF-MSN) composite is a sustainable, sensitive, and efficient material for both the detection and removal of Cu (II) ions from aqueous environments. Comprehensive characterization revealed a distinctive web-like structure of the nanofibers (average diameter, 33 nm), as well as uniform mesoporous silica nanoparticles (average particle size, 2 to 50 nm). Successful integration of CNF and MSN, with notable shifts and changes of the materials from the weak O–H stretching, which indicated hydrogen bonding between hydroxyl groups in CNF and surface silanol groups of the MSN in the CNF-MSN composite. The Griess-CNF-MSN composite enabled rapid and distinct colorimetric detection, achieving a linear response from 0.01 to 5 mg/L and an ultralow detection limit of 0.001521 mg/L, as determined using ImageJ. The results were validated by UV–Vis spectrophotometry. In terms of remediation, the CNF-MSN composite achieved nearly 100 % Cu(II) removal within 45 min at pH 4–6, outperforming its individual components. It reached a maximum adsorption capacity of 38.9 mg/g, with the adsorption equilibrium well described by the Dubinin-Radushkevich isotherm (R^2 = 0.980) and kinetics fitting a pseudo-second-order model (R^2 = 0.999). Real water sample tests confirmed its high removal efficiency, achieving 94.5 % in tap water, 98.1 % in deionized water, and 99.1 % in industrial wastewater. Overall, the CNF-MSN composite proves to be a green, low-cost, and multifunctional solution with excellent analytical performance and adsorption capacity, providing a powerful solution for the real-world detection and mitigation of heavy metal contamination in aquatic environments.

CRediT authorship contribution statement

Aneswa M. Ninela: Writing – original draft, Methodology, Investigation, Formal analysis, Data curation. **Sindisiwe F. Shange:** Writing – review & editing, Supervision, Project administration, Conceptualization. **Asanda Mtibe:** Writing – review & editing, Supervision, Resources, Conceptualization. **Jerome E. Andrew:** Resources, Methodology. **Thabang H. Mokhothu:** Writing – review & editing, Supervision, Project administration, Funding acquisition, Conceptualization.

Declaration of competing interest

The authors declare that they have no known competing financial interests or personal relationships that could have appeared to influence the work reported in this paper.

References

[1] A. Pandey, Pharmaceutical and biomedical applications of cellulose nanofibers: a review, Environ. Chem. Lett. 19 (2021) 2043–2055.
[2] M.C. Sheikh, M.M. Hasan, M.N. Hasan, M.S. Salman, K.T. Kubra, M.E. Awual, R. Waliullah, A.I. Rasee, A.I. Rehan, M.S. Hossain, Toxic cadmium (II) monitoring and removal from aqueous solution using ligand-based facial composite adsorbent, J. Mol. Liq. 389 (2023) 122854.
[3] A.H. Ragab, N.F. Gumaah, A.A. El Aziz Elfiky, M.F. Mubarak, Exploring the sustainable elimination of dye using cellulose nanofibrils-vinyl resin based nanofiltration membranes, BMC. Chem. 18 (2024) 121.
[4] H. Almasi, P. Jafarzadeh, L. Mehryar, Fabrication of novel nanohybrids by impregnation of CuO nanoparticles into bacterial cellulose and chitosan nanofibers: characterization, antimicrobial and release properties, Carbohydr. Polym. 186 (2018) 273–281.
[5] M.R.H. Khan, R.S. Hazra, G. Nair, J. Mohammad, L. Jiang, K. Reindl, M.K. Jawed, S. Ganai, M. Quadir, Cellulose nanofibers as scaffold-forming materials for thin film drug delivery systems, Int. J. Pharm. 627 (2022) 122189.
[6] T. Mokhena, M. John, Esterified cellulose nanofibres from sawdust using vegetable oil, Int. J. Biol. Macromol. 148 (2020) 1109–1117.
[7] P. Gupta, K.B Neelam, V. Sharma, Z. Azam, Applications of cellulose in biobased food packaging systems. Biobased Packaging Materials: Sustainable Alternative to Conventional Packaging Materials, Springer, 2024, pp. 101–124.
[8] C. Felgueiras, N.G. Azoia, C. Gonçalves, M. Gama, F. Dourado, Trends on the cellulose-based textiles: raw materials and technologies, Front. Bioeng. Biotechnol. 9 (2021) 608826.
[9] A. El Mahdaoui, S. Radi, A. Elidrissi, M.A.F. Faustino, M.G.P. Neves, N.M. Moura, Progress in the modification of cellulose-based adsorbents for the removal of toxic heavy metal ions, J. Environ. Chem. Eng. 12 (2024) 113870.
[10] A. Anžlovar, E. Žagar, Cellulose structures as a support or template for inorganic nanostructures and their assemblies, Nanomaterials 12 (2022) 1837.
[11] F.M. Shimizu, M.L. Braunger, A. Riul Jr, Heavy metal/toxins detection using electronic tongues, Chemosensors 7 (2019) 36.
[12] M.T. Hossain, S. Khandaker, M.M. Bashar, A. Islam, M. Ahmed, R. Akter, A. K. Alsukaibi, M.M. Hasan, H.M. Alshammari, T. Kuba, Simultaneous toxic Cd (II) and Pb (II) encapsulation from contaminated water using Mg/Al-LDH composite materials, J. Mol. Liq. 368 (2022) 120810.
[13] M.S. Hossain, M. Shenashen, M.E. Awual, A.I. Rehan, A.I. Rasee, R. Waliullah, K. T. Kubra, M.S. Salman, M.C. Sheikh, M.N. Hasan, Benign separation, adsorption, and recovery of rare-earth Yb (III) ions with specific ligand-based composite adsorbent, Process. Saf. Environ. Prot. 185 (2024) 367–374.
[14] A.A.E.A. Elfiky, M.F. Mubarak, M. Keshawy, I.E.T.E. Sayed, T.A. Moghny, Novel nanofiltration membrane modified by metal oxide nanocomposite for dyes removal from wastewater, Environ. Dev. Sustain. 26 (2024) 19935–19957.
[15] O.-A.O. Abiodun, O. Oluwaseun, O.K. Oladayo, O. Abayomi, A.A. George, E. Opatola, R.F. Orah, E.J. Isukuru, I.C. Ede, O.T. Oluwayomi, Remediation of heavy metals using biomass-based adsorbents: adsorption kinetics and isotherm models, Clean Technol. 5 (2023) 934–960.
[16] Q. Chen, J. Zheng, L. Wen, C. Yang, L. Zhang, A multi-functional-group modified cellulose for enhanced heavy metal cadmium adsorption: performance and quantum chemical mechanism, Chemosphere 224 (2019) 509–518.
[17] N.A. Fakhre, B.M. Ibrahim, The use of new chemically modified cellulose for heavy metal ion adsorption, J. Hazard. Mater. 343 (2018) 324–331.
[18] J. Kaur, P. Sengupta, S. Mukhopadhyay, Critical review of bioadsorption on modified cellulose and removal of divalent heavy metals (Cd, Pb, and Cu), Ind. Eng. Chem. Res. 61 (2022) 1921–1954.
[19] T. Mokhena, M. Mochane, A. Mtibe, S. Sigonya, B. Ntsendwana, E. Masibi, L. Sikhwivhilu, T. Motsoeneng, Recent advances on nanocellulose-graphene oxide composites: a review, Cellulose 31 (2024) 7207–7249.
[20] Z. Ali, R. Ullah, M. Tuzen, S. Ullah, A. Rahim, T.A. Saleh, Colorimetric sensing of heavy metals on metal doped metal oxide nanocomposites: a review, *Trends in Environ*, Anal. Chem. 37 (2023) e00187.
[21] J.C. Ragain, A review of color science in dentistry: colorimetry and color space, J. Dent. Oral Disord. Ther. 4 (2016) 1–5.
[22] S. Yılmaz, N. Ullah, D. Citak, B. Hazer, M. Tuzen, Vortex-assisted dispersive solid-phase microextraction of cadmium and copper on magnetic polystyrene-b-poly dimethyl siloxane hydrophobic block copolymer for their atomic absorption spectrometric determination in water, soft drink and food samples, J. Food Compos. Anal. 123 (2023) 105487.
[23] N. Hassan, A. Shahat, A. El-Didamony, M. El-Desouky, A. El-Bindary, Equilibrium, kinetic and thermodynamic studies of adsorption of cationic dyes from aqueous solution using ZIF-8, Mor. J. Chem. 8 (2020) 2627–2637. J. Chem. 8 (3) (2020).
[24] S.F. Muthwa, T.R. Makhanya, M. Mlambo, N.P. Shumbula, P.M. Shumbula, S. C. Onwubu, N. Moloto, R.M. Gengan, P.S. Mdluli, Synthesis and characterization of 3-(p-tolyl)-2, 3-dihydropyrazolo [3, 4-b] indole-1 (4H)-carbothioamide functionalized gold nanoparticles for the CIEL* a* b*/yxy colorimetric detection of Cr (VI), J. Mol. Struct. 1209 (2020) 127985.
[25] M.R. Luo, Cielab, Encyclopedia of Color Science and Technology, Springer, 2023, pp. 251–257.
[26] A. Waheed, M. Mansha, N. Ullah, Nanomaterials-based electrochemical detection of heavy metals in water: current status, challenges and future direction, Trends Anal. Chem. 105 (2018) 37–51.
[27] D. Tibaduiza, M. Anaya, J. Gómez, J. Sarmiento, M. Perez, C. Lara, J. Ruiz, N. Osorio, K. Rodriguez, I. Hernandez, Electronic tongues and noses: a general overview, Biosens 14 (2024) 190.
[28] S.E. Magubane, M. Mlambo, M.H. Mabaso, S.F. Muthwa, H.G. Kruger, P.S. Mdluli, Optimization of CIEL* a* b*/yxy colour system for colorimetric devices fabricated with gold nanoparticles, J. Mol. Struct. 1191 (2019) 271–277.
[29] A. Sadollahkhani, A. Hatamie, O. Nur, M. Willander, B. Zargar, I. Kazeminezhad, Colorimetric disposable paper coated with ZnO@ ZnS core–shell nanoparticles for detection of copper ions in aqueous solutions, ACS. Appl. Mater. Interfaces. 6 (2014) 17694–17701.
[30] A. Sadollahkhani, I. Kazeminezhad, J. Lu, O. Nur, L. Hultman, M. Willander, Synthesis, structural characterization and photocatalytic application of ZnO@ ZnS core–shell nanoparticles, RSC. Adv. 4 (2014) 36940–36950.
[31] G. Sharma, W. Wu, E.N. Dalal, The CIEDE2000 color-difference formula: implementation notes, supplementary test data, and mathematical observations, Color Res. Appl.: Endorsed Inter-Soc. Color Counc. Colour Group (G. B.) Can. Soc. Color Color Sci. Assoc. Jpn. Dutch Soc. Study Color Swed. Colour Cent. Found. Colour Soc. Aust. Cent. Fr. Coul. 30 (2005) 21–30.
[32] M.A. Ansari, D.K. Singh, Significance of color spaces and their selection for image processing: a survey, RACSC 15 (2022) 946–956.
[33] N.P. Kubheka, S.F. Shange, S.C. Onwubu, N. Deenadayalu, P.S. Mdluli, T. H. Mokhothu, ImageJ analysis for quantifying lead ion in environmental water using gold nanoparticles as a colorimetric probe, J. Mol. Liq. 420 (2025) 126804.
[34] T.H. Mokhothu, A.S. Luyt, M. Messori, Preparation and characterization of EPDM/silica composites prepared through non-hydrolytic sol-gel method in the absence and presence of a coupling agent, Express. Polym. Lett. 8 (2014) 809–822.
[35] T. Taweekarn, W. Wongniramaikul, W. Limsakul, W. Sriprom, C. Phawachalotorn, A. Choodum, A novel colorimetric sensor based on modified mesoporous silica nanoparticles for rapid on-site detection of nitrite, Microchim.. Acta 187 (2020) 1–13.
[36] B. Sahu, R. Kurrey, M.K. Deb, K. Shrivas, I. Karbhal, B.R. Khalkho, A simple and cost-effective paper-based and colorimetric dual-mode detection of arsenic (iii) and lead (ii) based on glucose-functionalized gold nanoparticles, RSC. Adv. 11 (2021) 20769–20780.
[37] D.J. Soldat, P. Barak, B.J. Lepore, Microscale colorimetric analysis using a desktop scanner and automated digital image analysis, J. Chem. Educ. 86 (2009) 617.
[38] B. Zandi, T.Q. Khanh, Towards intelligent illumination systems: from the basics of light science to its application, Z. Arb. Wiss. 77 (2023) 126–144.
[39] M.I. Kurki, J. Karjalainen, P. Palta, T.P. Sipilä, K. Kristiansson, K.M. Donner, M. P. Reeve, H. Laivuori, M. Aavikko, M.A. Kaunisto, FinnGen provides genetic insights from a well-phenotyped isolated population, Nature 613 (2023) 508–518.
[40] H. Zhang, R. Li, Y. Ling, R. Zhang, G. Zhu, G. Fu, Y. Tang, Efficient Colorimetry: Developing an Application to Support Student Digital Colorimetry Experiments, ACS Publications, 2024.
[41] T.-Y. Ou, C.-F. Lo, K.-Y. Kuo, Y.-P. Lin, S.-Y. Chen, C.-Y. Chen, Visual Cu2+ detection of gold-nanoparticle probes and its employment for Cu^{2+} tracing in circuit system, Nanoscale Res. Lett. 17 (2022) 104.
[42] M.R. Awual, M.M. Hasan, Colorimetric detection and removal of copper (II) ions from wastewater samples using tailor-made composite adsorbent, Sens. Actuator B-Chem. 206 (2015) 692–700.
[43] I. Langmuir, The adsorption of gases on plane surfaces of glass, mica and platinum, J. Am. Chem. Soc. 40 (1918) 1361–1403.
[44] H. Freundlich, Adsorption in solution, J. Phys. Chem. (1906) 1361–1368.
[45] M. Dubinin, Porous structure of adsorbents and catalysts, Adv. Colloid. Interface Sci. 2 (1968) 217–235.
[46] Y.-S. Ho, G. McKay, Pseudo-second order model for sorption processes, Process. Biochem. 34 (1999) 451–465.
[47] D. Dhaneswara, J.F. Fatriansyah, F.W. Situmorang, A.N. Haqoh, Synthesis of amorphous silica from rice husk ash: comparing HCl and CH_3COOH acidification methods and various alkaline concentrations, Synth 11 (2020) 200–208.
[48] M. Pranjic, Investigation of the Effects of Enzymatic Hydrolysis and Hydroxylation on Oriented Semi-Crystalline Cellulose by Ex Situ Polarisation Dependent Raman Spectroscopy, University of York, 2021.
[49] T. Kant, K. Shrivas, A. Tejwani, K. Tandey, A. Sharma, S. Gupta, Progress in the design of portable colorimetric chemical sensing devices, Nanoscales 15 (2023) 19016–19038.
[50] X. Xie, Z. Zhu, Y. Meng, L. Wang, F. Zhao, L. Chen, L. Jiang, M. Yan, X. Zhou, Ambient-dried silica xerogels with enhanced strength and thermal insulation via calcium ion-glycerol synergistic crosslinking, Gels. 11 (2025) 462.
[51] N.N. Maseko, D. Enke, S.A. Iwarere, O.S. Oluwafemi, J. Pocock, Synthesis of low density and high purity silica xerogels from South African sugarcane leaves without the usage of a surfactant, Sustainability 15 (2023) 4626.
[52] M.T. Mazibuko, S.C. Onwubu, P.S. Mdluli, V. Paul, M.C. Teboho, M. Thabang, Amine-functionalized cellulose-silica composites for the remediation of hexavalent chromium (Cr IV) in contaminated water, Res. Chem. 11 (2024) 101796.
[53] L. Usgodaarachchi, C. Thambiliyagodage, R. Wijesekera, M.G. Bakker, Synthesis of mesoporous silica nanoparticles derived from rice husk and surface-controlled amine functionalization for efficient adsorption of methylene blue from aqueous solution, CRGSC 4 (2021) 100116.
[54] A.I. Rasee, E. Awual, A.I. Rehan, M.S. Hossain, R. Waliullah, K.T. Kubra, M. C. Sheikh, M.S. Salman, M.N. Hasan, M.M. Hasan, Efficient separation, adsorption,

and recovery of samarium (III) ions using novel ligand-based composite adsorbent, Surf. Sci. 41 (2023) 103276.
[55] S.S. Gabr, M.F. Mubarak, M. Keshawy, I.E.T. El Sayed, T. Abdel Moghny, Linear and nonlinear regression analysis of phenol and P-nitrophenol adsorption on a hybrid nanocarbon of ACTF: kinetics, isotherm, and thermodynamic modeling, Appl. Water. Sci. 13 (2023) 230.
[56] X.-Q. Cheng, Z.-H. Dai, H.-X. Gao, Q.-S. Pan, X.-J. Kong, F.-F. Shen, S. Wu, Dual-readout assay for determination of Ag^{+} and Cu^{2+} based on in situ fluorogenic and chromogenic reaction between dopamine and naphthoresorcin, Microchem. J. 196 (2024) 109591.
[57] Y. Wang, L. Wang, Z. Su, J. Xue, J. Dong, C. Zhang, X. Hua, M. Wang, F. Liu, Multipath colourimetric assay for copper (II) ions utilizing MarR functionalized gold nanoparticles, Sci. Rep. 7 (2017) 41557.
[58] R.J. Tilley, Colour and the Optical Properties of Materials, John Wiley & Sons, 2020.
[59] M.R. Awual, M.M. Hasan, J. Iqbal, M.A. Islam, A. Islam, S. Khandaker, A.M. Asiri, M.M. Rahman, Ligand-based sustainable composite material for sensitive nickel (II) capturing in aqueous media, J. Environ. Chem. Eng. 8 (2020) 103591.
[60] M.M. Hasan, K.T. Kubra, M.N. Hasan, M.E. Awual, M.S. Salman, M.C. Sheikh, A. I. Rehan, A.I. Rasee, R. Waliullah, M.S. Islam, Sustainable ligand-modified based composite material for the selective and effective cadmium (II) capturing from wastewater, J. Mol. Liq. 371 (2023) 121125.
[61] F.I. Abouzayed, N.T.A. El-Nassr, S.A. Abouel-Enein, Synthesis, characterization of functionalized grafted cellulose and its environmental application in uptake of copper (II), manganese (II) and iron (III) ions, J. Mol. Struct. 1270 (2022) 133907.
[62] A. Shahat, K.T. Kubra, A. El-marghany, Equilibrium, thermodynamic and kinetic modeling of triclosan adsorption on mesoporous carbon nanosphere: optimization using Box-Behnken design, J. Mol. Liq. 383 (2023) 122166.
[63] M.R. Awual, I.M. Rahman, T. Yaita, M.A. Khaleque, M. Ferdows, pH dependent Cu (II) and Pd (II) ions detection and removal from aqueous media by an efficient mesoporous adsorbent, Chem. Eng. J. 236 (2014) 100–109.
[64] Q. Wu, H. He, H. Zhou, F. Xue, H. Zhu, S. Zhou, L. Wang, S. Wang, Multiple active sites cellulose-based adsorbent for the removal of low-level Cu (II), Pb (II) and Cr (VI) via multiple cooperative mechanisms, Carbohydr. Polym. 233 (2020) 115860.
[65] M. Hemdan, A.H. Ragab, S.S. Elyan, M.A. Taher, M.F. Mubarak, Eco-friendly activated carbon thin film-zeolitic imidazolate framework-8 (ACTF@ ZIF-8) nanocomposite for efficient methylene blue removal: synthesis, characterization, and adsorption performance, J. Clust. Sci. 36 (2025) 2.
[66] I. Ahmed, K.K. Adhikary, Y.-R. Lee, K.H. Row, K.-K. Kang, W.-S. Ahn, Ionic liquid entrapped UiO-66: efficient adsorbent for Gd^{3+} capture from water, Chem. Eng. J. 370 (2019) 792–799.
[67] Y. Zhang, W. Guo, D. Liu, J. Xu, Rational design of novel carboxylic acid functionalized phosphonium based ionic liquids as high-performance extractants for rare earths, J. Rare Earths 39 (2021) 1435–1441.
[68] Z. Sun, Y.-G. Chen, X. Mu, D.-B. Wu, W.-M. Ye, Graphene oxide-modified organic Gaomiaozi bentonite for Yb (III) adsorption from aqueous solutions, Mater. Chem. Phys. 274 (2021) 125176.
[69] A.A.E.A. Elfiky, M.F. Mubarak, M. Keshawy, I.E.T.E. Sayed, T.A. Moghny, Removing of cationic dyes using self-cleaning membranes-based PVC/nano-cellulose combined with titanium aluminate, Environ. Sci. Pollut. Res. 30 (2023) 79091–79105.
[70] M.F. Mubarak, H. Selim, R. Elshypany, Hybrid magnetic core–shell TiO2@ $CoFe_3O_4$ composite towards visible light-driven photodegradation of methylene blue dye and the heavy metal adsorption: isotherm and kinetic study, J. Environ. Health Sci. Eng. 20 (2022) 265–280.